Biomaterials 33 (2012) 20–28

Contents lists available at SciVerse ScienceDirect

Biomaterials

journal homepage: www.elsevier.com/locate/biomaterials

# Topographic control of the growth and function of cardiomyoblast H9c2 cells using nanodot arrays

Hsu-An Pan[a], Yao-Ching Hung[b,c], Yu-Ping Sui[a], G. Steve Huang[a,*]

[a] Graduate Program for Nanotechnology, Department of Materials Science and Engineering, National Chiao Tung University, 1001 Ta-Hsueh Road, Hsinchu, Taiwan 300, ROC
[b] College of Medicine, China Medical University, Taichung, Taiwan 40402, ROC
[c] Department of Obstetrics & and Gynecology, China Medical University Hospital, Taichung, Taiwan 40402, ROC

ARTICLE INFO

*Article history:*
Received 18 August 2011
Accepted 21 September 2011
Available online 6 October 2011

*Keywords:*
Nanotopography
Cell proliferation
Focal adhesion
Cardiomyoblast
Hypertrophy
Cardiovascular stent

ABSTRACT

Cardiovascular stents require optimised control for the enhancement or inhibition epithelial and smooth muscle cell growth in close contact with the implant. Here we propose that the surface topology in contact with the living cells could be designed to control and optimise the growth and function of such cells. The cardiomyoblast H9c2 was cultured on nanodot arrays with dot diameters ranging between 10 and 200 nm. On the 50-nm nanodot arrays H9c2 showed maximum attachment and proliferation with largest cell area and extended lamellipodia. In contrast, 53.7% and 72.6% reductions of growth were observed on the 100- and 200-nm nanodot arrays after 3 days. Immunostaining indicated that nanodots smaller than 50-nm induced cell adhesion and cytoskeleton organization. Expression of genes associated with fibrosis and hypertrophy was up-regulated in cells grown on 100-nm nanodots. Western blot data showed high levels of expression for vinculin and plasminogen activator inhibitor-1 for cells cultured on 50-nm nanodots. Nanotopography controls cell adhesion, morphology and proliferation. By adjusting the diameter of the nanodots, we could modulate the growth and expression of function-related genes and proteins of H9c2 cardiomyoblasts. The current study provides insights for improved design of artificial implants and parameters that affect biocompatibility.



## 1. Introduction

Control of cell proliferation, adhesion, and function at the biosurface interface is essential for the long-term stability of cardiovascular implants [1]. Conventional metals are generally not compatible with tissues. This poor biocompatibility can cause acute thrombosis and long-term restenosis. As a result, the metallic stent can fail due to the response of the vascular smooth muscle cells (VSMCs) or decreased function of the endothelial cells in the vessel [2]. A frequently used approach to improve the biocompatibility of the vascular stent is to coat the traditional metallic surface with materials such as hyaluronan [3], tantalum [4], expanded polytetrafluoroethylene [5], or silicon carbide [6]. These surface modifications all help improve the biocompatibility of the stent with the VSMCs and decrease the interactions of the vascular stent with blood cells. Other options have been suggested to alter the original surface of the metallic vascular stents to enable them to interact with cells [7]. The modification of physical structure may be beneficial in the long-term to design of artificial implants.

The surface topology at the nanoscale encodes information that directs cell behaviour [8]. Increasing evidence indicates that physical structures affect cell behaviour by providing scaffolds and interacting with the integrins on the cell membrane. Nanoscale texture generated through the deposition of nanocoatings may be useful to improve biocompatibility because surface topography can promote vascular smooth muscle cell and endothelial cell adherence and proliferation [9,10].

Cells have been grown on a variety of nanoscale textures that elicit a broad range of responses. To decode the 3-dimensional (3D) structural information, cells have been cultured on nano-scaled structures including nanoislands [11], nanopits [12], nanoneedles [13], and nanoposts [14]. In addition, cells have also been grown on random structures such as nanofibers or metal surfaces that mimic the native structure of the extracellular matrix. In general, increased cell adhesion, proliferation, long-term adhesion, cytoskeletal organisation, and extracellular matrix remodelling were observed in cells cultured on 13 nm diameter nanoislands [15]. Decreases in cytoskeleton organisation were observed in human fibroblasts (hTERT-BJ1) cultured on nanocolumns (100 nm in diameter and between 160 and 170 nm high) [16]. Nanorods and nanoposts seem to inhibit cell proliferation and adhesion. Less cell adhesion and

* Corresponding author.
*E-mail address:* gstevehuang@mail.nctu.edu.tw (G.S. Huang).

0142-9612/$ – see front matter © 2011 Elsevier Ltd. All rights reserved.
doi:10.1016/j.biomaterials.2011.09.054

lower viability were observed in umbilical vein and capillary endothelial cells cultured on ZnO nanorods [17]. The needle-like silicon nanoposts reduced cellular proliferation of fibroblasts [18]. A 3D nanofibrillar surface composed of electro-spun polyamide nanofibers promoted the proliferation and self-renewal of mouse embryonic stem cells [19]. The correlation of nanotopography with cell growth and function has not been clearly demonstrated.

The biocompatibility of stents requires design optimisation. The biocompatible material gold is thought to be ideal for coating coronary stents because of its radio-opaque properties [20]. Some studies evaluating the biocompatibility of gold-coated stents suggest that they are equivalent to uncoated steel stents [21]. However, other studies, albeit with patients enrolled who were at higher risk for restenosis, concluded that these stents may increase neointimal hyperplasia compared to uncoated stents [22]. Silicon carbide is an inert semiconductor that can also be coated onto prosthetic surfaces and has been known to be relatively biocompatible and hemocompatible in *in vitro* studies [23]. Stents coated with silicon carbide also appear to be less thrombogenic than bare metal stents when implanted in human coronary arteries [24]. Overall, observational studies examining gold-coated stents show conflicting results, and the restenosis rates are no better than those obtained with uncoated steel stents [25].

In addition to biocompatibility, cellular function is another important concern in the design of artificial implants [26]. Biocompatibility does not guarantee optimal cell function. In many situations, biocompatibility must be balanced with cell function, such as when stimulation of VSMC proliferation causes restenosis in cardiovascular stents. Restenosis results from the proliferation of smooth muscle cells in the vessel wall in response to acute vessel wall injury induced by angioplasty. Recurrent stenosis and late-stage thrombosis remain significant limitations to successful stent function after stenting peripheral or coronary atherosclerotic lesions [27]. A nanotopographical platform with continuously varied structure could help achieve an implant surface topography that balances biocompatibility and function.

We fabricated arrays of nanodot surfaces containing dot diameters ranging between 10 and 200 nm. These nanodot arrays were used to acquire parameters for cell growth and the evaluation of the stage and grade of cancer cells [28]. This study surveyed the growth and function of H9c2 cardiomyoblasts using arrays of continuously varying nanotopography. We determined the nanostructure that achieved maximum cell growth and adhesion. Functional performance, indicated by the expression of representative genes, indicated that the optimised range of nanostructures derived balanced high biocompatibility and cell function.

## 2. Materials and methods

### 2.1. Cell culture

To eliminate possible contamination with nanometer- or micrometer-sized particles, the cell culture was performed in a class 10 clean room. H9c2 rat cardiomyoblasts were purchased from BCRC (Bioresource Collection and Research Center, Hsinchu, Taiwan) and cultured on various nanodot arrays with Dulbecco's Modified Eagle's Medium (DMEM) containing 10% fetal bovine serum (FBS, Gibco) and supplemented with 4 mM L-glutamine at 37 °C in a humidified 5% $CO_2$ incubator.

### 2.2. Chemicals

Glutaraldehyde and osmium tetroxide were purchased from Electron Microscopy Sciences (USA). Anti-vinculin mouse antibody was purchased from Abcam (USA). Alexa Fluor 594 phalloidin and Alexa Fluor 488 goat anti-mouse IgG were purchased from Invitrogen (USA). Trypsin was purchased from Sigma (USA). Bromodeoxyuridine drug and antibody were purchased from Millipore. Other chemicals of analytical grade or higher were purchased from Sigma or Merck. Anti-β-actin mouse antibody and anti-plasminogen activator inhibitor-1 (PAI-1) rabbit antibody were purchased from Novus. High levels of PAI-1 are associated with an increased risk of thromboembolic disease.

### 2.3. Fabrication of nanodot arrays

Nanodot arrays were fabricated as previously described [29]. A TaN thin film 150 nm thick was sputtered onto a 6 inch silicon wafer, followed by deposition of a 3 μm thick aluminium layer on top of the TaN thin film. Anodisation was performed using either a 1.8 M sulphuric acid solution at 5 V for the 10-nm nanodot array or a 0.3 M oxalic acid solution at 25 V, 60 V, or 100 V for the 50-, 100-, or 200-nm nanodot arrays, respectively. Porous anodic alumina was formed during the anodic oxidation. The underlying TaN layer was oxidised into tantalum oxide nanodots using the alumina nanopores as a template. The porous alumina was then removed by immersing the array in a 5% (w/v) $H_3PO_4$ solution overnight. The dimension and homogeneity of the nanodot arrays were measured or calculated from images taken using a JEOL JSM-6500 TFE-SEM.

### 2.4. Measurement of cell attachment by cell density

Cells were double stained using 4′,6-diamidino-2-phenylindole DAPI and phalloidin. H9c2 cells were harvested and fixed using 4% paraformaldehyde diluted in PBS for 30 min, followed by 3 washes in PBS. Cell membranes were permeabilised during 10 min incubation in 0.1% Triton X-100, followed by 3 PBS washes. H9c2 cells were incubated with phalloidin and nuclei counterstained with DAPI for 15 min at room temperature. Samples were mounted and imaged using a Leica TCS SP2 confocal microscope. Cell number was counted using ImageJ software and expressed in terms of cell density.

### 2.5. Scanning electron microscopy (SEM)

Harvested cells were fixed using 1% glutaraldehyde in PBS at 4 °C for 20 min, followed by post-fixation in 1% osmium tetraoxide for 30 min. Ethanol dehydration was performed using a series of 10 min incubations in 50, 60, 70, 80, 90, 95, and 100% ethanol and air dried. The specimen was sputter-coated with platinum and examined by JEOL JSM-6500 TFE-SEM at an accelerating voltage of 5 keV.

### 2.6. Immunostaining

Cells were harvested and fixed using 4% paraformaldehyde in PBS for 15 min followed by 3 PBS washes. Cell membranes were permeabilised using 0.1% Triton X-100 incubation for 10 min, followed by 3 washes in PBS. The membranes were then blocked using 1% BSA in PBS for 1 h and washed again in PBS 3 times. The sample was incubated with anti-vinculin antibody (diluted in 1% BSA solution) and phalloidin for 1 h, followed by incubation with Alexa Fluor 488 goat anti-mouse antibody for 1 h and then 3 washes in PBS. Samples were mounted and imaged using a Leica TCS SP2 confocal microscope.

### 2.7. Bromodeoxyuridine (BrdU) proliferation assay

H9c2 cells were incubated with BrdU drug for 6 h prior to harvest. Cells were then harvested and fixed using 4% paraformaldehyde in PBS for 15 min followed by 3 PBS washes. Cell membranes were permeabilised using 10 min incubation in 0.1% Triton X-100, followed by 3 PBS washes. A 2N HCl solution was applied to break the nuclear membranes. Next, cells were blocked using 1% BSA in PBS for 1 h. Cells were incubated with anti-BrdU antibody (diluted in 1% BSA) for 24 h at 4 °C, followed by incubation with Alexa Fluor 488 goat anti-mouse antibody and DAPI for 1 h and then 3 washes in PBS. H9c2 cells were then counterstained using BrdU and DAPI to image the nucleus. Samples were mounted and imaged using a Leica TCS SP2 confocal microscope. ImageJ software was used to determine BrdU-labelled cell numbers.

### 2.8. Western blot

Cultured H9c2 cardiomyoblasts were lysed and centrifuged at 12000 g for 2 min at 4 °C. The supernatants were transferred to new Eppendorf tubes and protein concentrations were defined using UV/VIS spectroscopy. After the protein concentrations were defined, solutions were mixed with 4X sample buffer and lysis buffer to a final concentration of 1 μg/μL protein. Samples were heated at 95 °C for 3 min and cooled at 0 °C for 3 min; this step was repeated twice. Proteins were separated using 10% SDS-PAGE gels and transferred to PVDF membranes. Nonspecific protein binding was blocked using a 5% milk solution at 4 °C overnight. The membranes were subsequently blotted at 4 °C overnight using the specific antibodies indicated for each experiment, which were diluted in blocking buffer. Specific primary antibodies were blotted using second antibodies in the blocking buffer at room temperature for 1 h. Chemiluminescent detection was performed using western blotting luminol reagent and oxidising reagent (U.S.A.).

### 2.9. Quantitative real-time PCR

Oligo primers used to amplify genes of interest were designed based on the sequences provided in previous reports [30–32](Table 1). The specificity of synthesised primers was verified by polymerase chain reaction (PCR) using reverse-transcribed mRNA extracted from H9c2 cells as a template. The sizes of PCR products were resolved using agarose gel electrophoresis.

**Table 1**
Primer sequences.

| Gene | Forward sequence | Reverse sequence |
|---|---|---|
| GAPDH | gcctacctcatgggactgaa | acattctgccctttggtgac |
| Hsp27 | gagtggtctcagtggttcag | ccttccttggtcttaactgtg |
| Hsp60 | acaagtgatgttgaagtgaatg | atgcaggaattttaagtgctc |
| Hsp70 | cctacttcaacgactcgcag | cttcctcttgaactcctccac |
| Hsp90 | gtcttctctcgcttctcactt | vtatctgtgggaggggattct |
| beta-MHC | gcctacctcatgggactgaa | acattctgccctttggtgac |
| **GATA-4** | agaaggcagagagtgtgtca | cagtgtggtggtggtagtct |
| PAI-1 | gaacgccctctattgtgccgaac | ctctgttggattgtgccgaac |
| ANF | tgggctccttctccatcacc | gccaaaaggccaggactgac |
| RAMP2 | ttactgctgctgttgctgct | aggaaagggatgaggcagat |
| RAMP3 | acctggtcgtgtcaaagtcc | ccacaccttccagatgacct |
| Bcl-2 | gctacgagtgggatactgg | gtgtgcagatgccggttca |
| Bax | ctgcagaggatgattgctga | gatcagctcgggcactttag |

Total RNA was extracted from $1.8 \times 10^5$ cells using TRI-reagent (Talron Biotech) according to the manufacturer's specifications. The RNA was isolated using chloroform extraction and isopropanol precipitation. The RNA extract was immediately purified using an RNeasy Mini Kit (Qiagen) to remove impurities and unwanted organic compounds. Purified RNA was resuspended in DEPC-treated water and quantified by $OD_{260}$. The $OD_{260}$-to-$OD_{280}$ ratio usually exceeded 2.0 at this stage. For cDNA synthesis, 1 μg total RNA was annealed using 1 μg oligo-dT primer, followed by reverse transcription using SuperScript® III Reverse Transcriptase (Invitrogen) in a total volume of 50 μl. Between 0.2 and 0.5 μl of the reverse transcription reactions were used for quantitative qPCR using SYBR Green I performed on an iCycler iQ5 (Bio-Rad Laboratories). The cycling conditions were as follows: 1 cycle of 5 min at 95 °C and 50 cycles of 20 s at 95 °C, 20 s at 55 °C, and 40 s at 72 °C. Fluorescence was measured after each 72 °C step. Expression levels were obtained using threshold cycles (Ct) that were determined by the iCycler iQ Detection System software. Relative transcript quantities were calculated using the ΔΔCt method. The gene GAPDH was used as a reference gene and was amplified along with the target genes from the same cDNA samples. The difference in threshold cycles of the sample mRNA relative to GAPDH mRNA was defined as the ΔCt. The difference between the ΔCt of the control cells and the ΔCt of the cells grown on nanodot arrays was defined as the ΔΔCt. The fold change in mRNA expression was expressed as $2^{\Delta\Delta Ct}$. The results were expressed as the mean ± SD of six experiments.

### 2.10. Statistics

The means and standard deviations were calculated for the recorded data. Student's *t*-test was employed to determine data sets that differed significantly from one another, and significance was defined as a $p$-value $< 0.05$.

## 3. Results and Discussions

### 3.1. Cell attachment and proliferation of cardiomyoblasts grown on arrays of nanodots

Nanodot arrays with dot diameters of 10-, 50-, 100-, or 200-nm were fabricated as described previously by anodic aluminium oxide

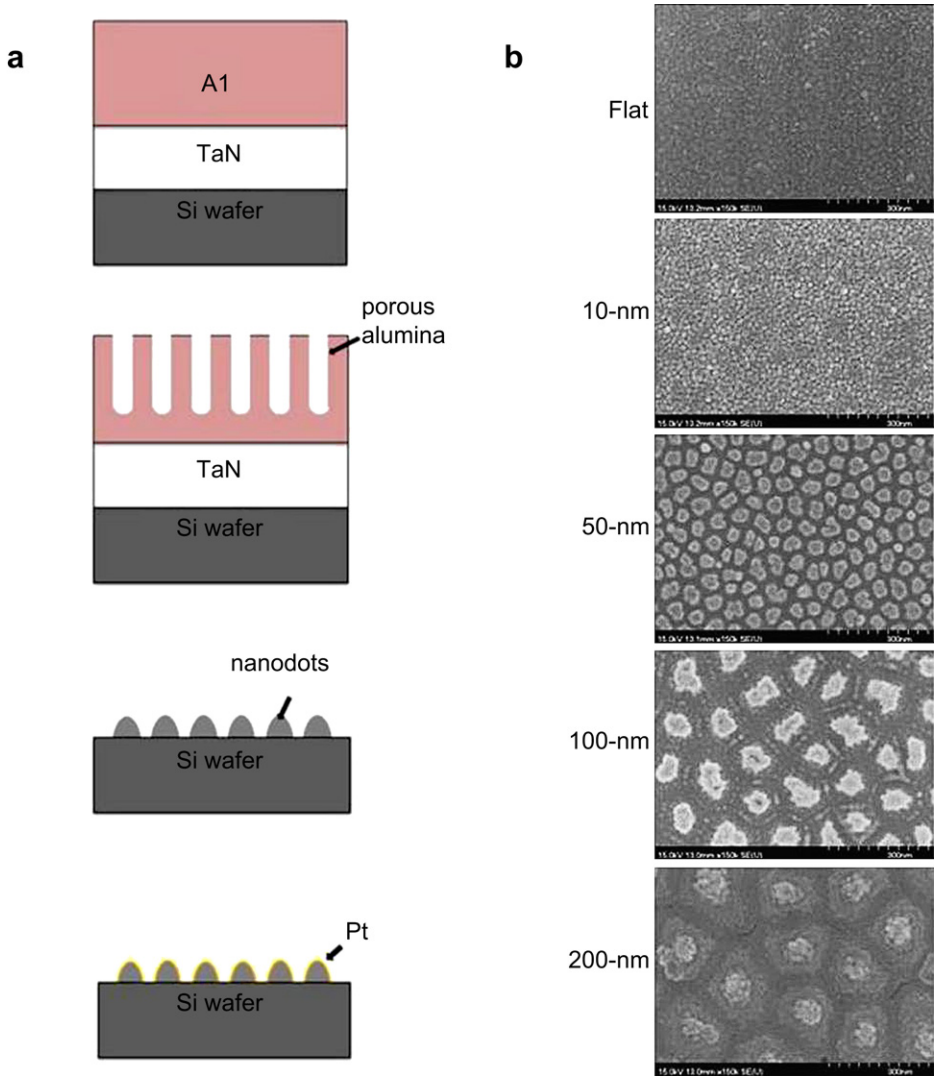


**Fig. 1.** Tantalum-based nanodot arrays fabricated using AAO processing. (a) Schematic representation of the fabrication of nanodot arrays. (b) High resolution scanning electron micrographs of nanodot surfaces: flat surfaces and 10-, 50-, 100-, or 200-nm diameter nanodots. Scale bar = 300 nm.

(AAO) processing on tantalum-coated wafers [33]. The nanodot diameters were 15 ± 2.8, 58.1 ± 5.6, 95.4 ± 9.2, or 211.5 ± 30.6 nm for 10-, 50-, 100-, or 200-nm dot arrays, respectively (Fig. 1a,b). The average nanodot height for each array was 11.3 ± 2.5, 51.3 ± 5.5, 101.1 ± 10.3, and 154.2 ± 27.8 nm, respectively. The distance between dots was 22.8 ± 4.6, 61.3 ± 6.4, 108.1 ± 2.3, or 194.2 ± 15.1 nm, respectively (Pan et al., 2009). In all cases, dimensions of the nanodots were tightly controlled and well defined.

To evaluate the attachment level of cardiomyoblasts to various nanodot arrays, H9c2 cardiomyoblasts were cultured on fabricated nanodot arrays or on flat wafers at densities between 2000 and 5000 cells per square centimetre. Cells were harvested 24 h (day 1), 72 h (day 3), and 120 h (day 5) after seeding. DAPI staining was performed to identify viable cells. Immunostaining using anti-actin filament IgG was performed to verify the normal growth state of cells stained by DAPI. The density of viable cells was obtained by counting DAPI-stained cells (Fig. 3a). On day 1, most cells cultured on the 10-, 50-, or 100-nm nanodot arrays grew well, and the densities of cells cultured on arrays were comparable that on flat controls. In contrast, at day 1, cells cultured on the 200-nm nanodot arrays exhibited a 64.9% reduction in cell number compared to a flat surface. On day 3, an increase in cell viability was generally observed for cells cultured on flat, 10-nm, and 50-nm nanodot surfaces; however, there is a 53.7% and 72.6% reduction, respectively, in cell densities observed on the 100- and 200-nm nanodot arrays. The reduction in cell number observed on day 5 for flat surfaces and 10-nm nanodot arrays is apparently due to the overgrowth of cells, which occupied more than 90% of the culture dish surface area rather than to the nanotopology of the surface. On day

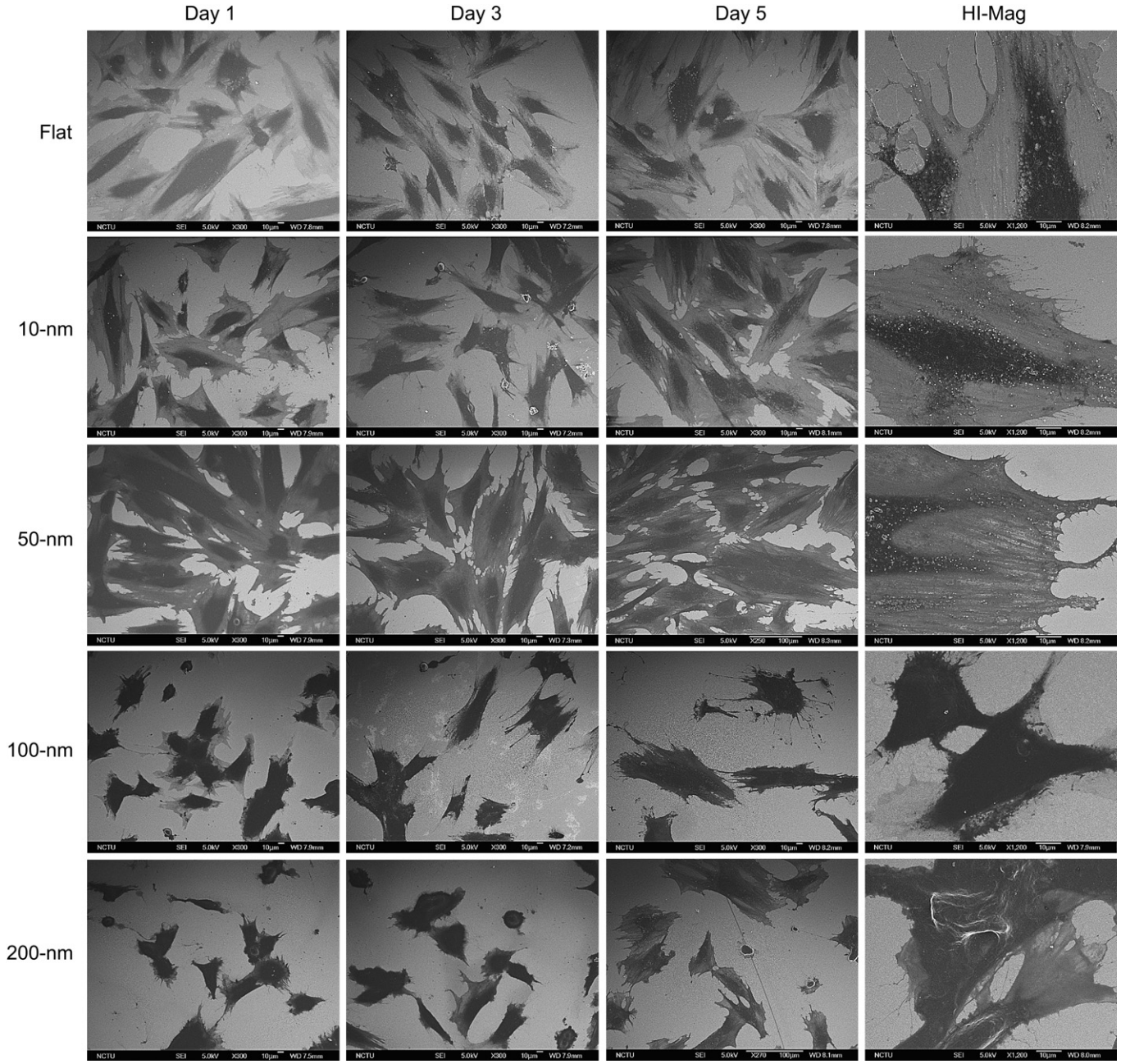


**Fig. 2.** Morphology of H9c2 cardiomyoblasts cultured on nanodot arrays using SEM. H9c2 cells are grown on flat, 10-, 50-, 100-, and 200-nm nanodot arrays for either 1, 3, or 5 days. High magnification SEM images (Hi-Mag) show lamellipodia present in cells cultured on flat, 10-, 50-, 100-, or 200-nm nanodot arrays for 3 days. Scale bar = 10 μm.

5, cells cultured on the 100- or 200-nm nanodot arrays exhibit a small increase in the viability of cells compared to day 3 and day 1, but a significant retardation of growth when compared to flat surfaces.

Bromodeoxyuridine (BrdU) cell proliferation assay is a non-isotopic immunoassay for quantification of newly synthesised DNA in actively proliferating cells. BrdU was applied to differentiate the newly proliferated cells from pre-existing culture. Additionally, DAPI was used to stain the nuclei, an indicator of the total number of viable cells (Fig. 3b). On day 1, maximum proliferation was observed in cells grown on 50-nm nanodot arrays, which was approximately 2-fold greater than cells grown on flat surfaces. On day 3, significant proliferation is still observed; the reduction in growth rate is likely due to the saturation of cells.

In summary, optimal growth occurred on 50-nm nanodot arrays. These permitted maximum cell attachment even when the cell density reached saturation. On flat surfaces and 10-nm nanodots, cardiomyoblasts grew well; however, a minor decrease in cell density was observed on day 5 when cells were grown to saturation. Nanodots of 100- and 200-nm prevented viable growth of cardiomyoblasts, as indicated by 53.7% and 72.6% reductions, respectively, on day 3. Maximum proliferation occurred in cells grown on 50-nm nanodots, which was approximately 2-fold more than cells grown on flat surfaces.

### 3.2. Nanotopography-modulated morphology of cardiomyoblasts

Morphology is an important index for cell growth. Flat and extended cells indicate healthy and proliferate growth. Nanotopography is known to modulate cell morphology of NIH-3T3 cells [29]. Biochemical and genetic evidence indicated that apoptosis occurs in cells with abnormal morphology.

SEM was performed to examine the morphology of cells (Fig. 2). Cells grown on the flat surface and 10-nm nanodot arrays exhibited flat and extended conformation during the course of 5 days. Cells grown on 50-nm nanodot arrays showed more extended morphology and apparently larger surface area for each cell compared to those cultured on flat surfaces. Cells grown on 100-nm nanodot arrays exhibited distorted morphology with reduced cell adhesive area. The apoptosis-like appearance and reduction in surface area are most enhanced for cells seeded on the 200-nm nanodot arrays.

The morphology of cells clearly varied when cultured on arrays of differently sized nanodots. The variation in morphology also depended on incubation time. The surface area of cells grown on nanodots was measured and compared to that of cells grown on flat surfaces (Fig. 3c). On day 1, a 2-fold increase in surface area for cells grown on 50-nm nanodots was observed relative to flat surfaces. On day 3, a significant increase in the surface area of cells cultured

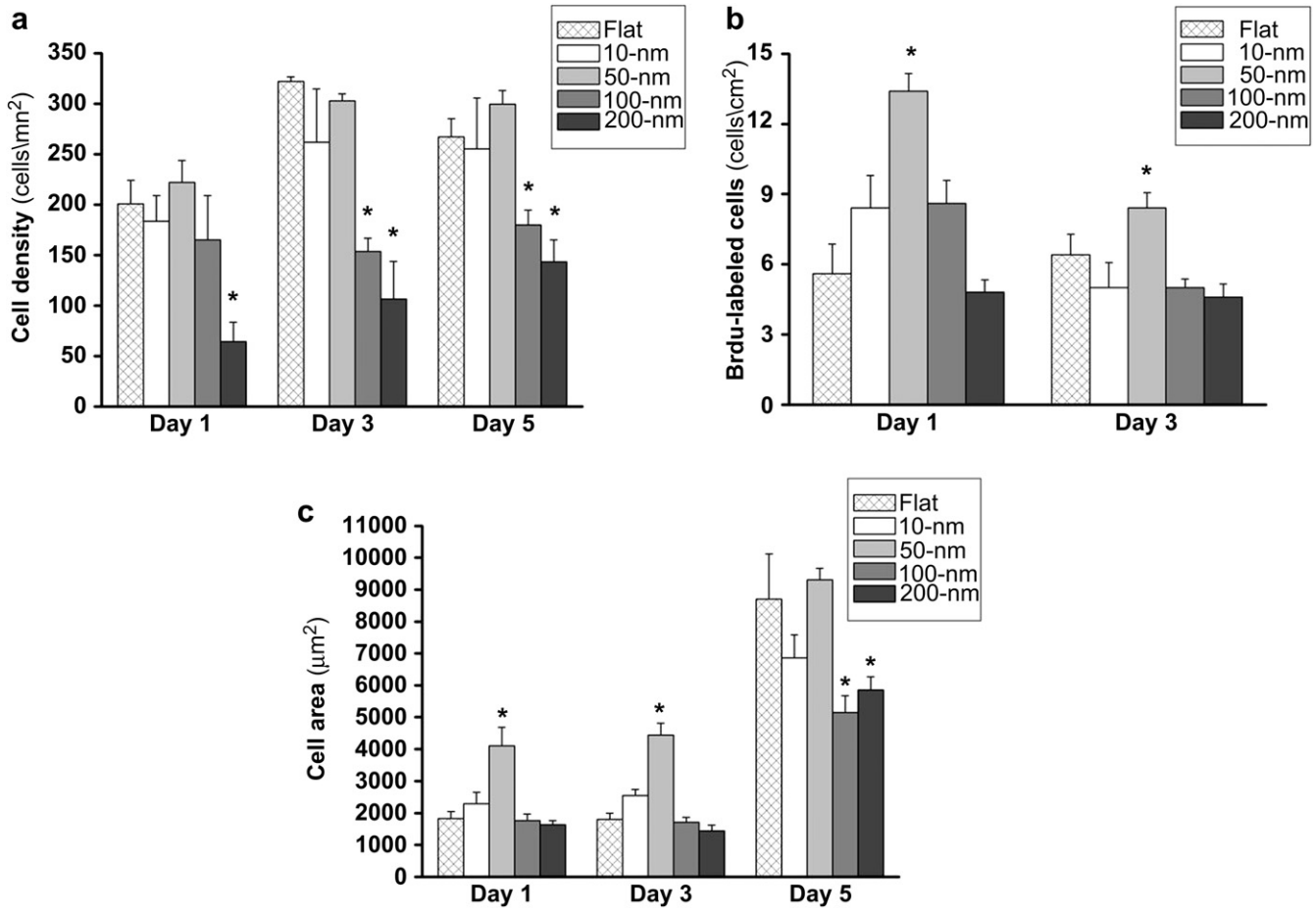


**Fig. 3.** Time course experiments to determine the dependence on nanotopography of cell density, proliferation, and cell spreading area of H9c2 cardiomyoblasts. Cardiomyoblasts seeded on nanodot arrays of various sizes were harvested after 1, 3, or 5 days culture. (a) Bar chart of cell density versus different sizes of nanodots. Cells were double-stained using DAPI and phalloidin. Cell density was calculated based on cell number counts. (b) Bar chart of proliferation versus dot size. Cells were incubated with BrdU and stained with a mouse anti-BrdU monoclonal antibody for 6 h and subsequently examined under a fluorescence microscope. Newly proliferated cells were also counted. (c) Plot of cell spreading area versus dot size. Cell spreading area was determined using SEM images of 50 cells per condition. The mean ± SD from at least 3 experiments is shown. *$p < 0.05$ when compared with flat control surfaces.

on 10- and 50-nm nanodot arrays was observed. The increase in surface area was not present on day 5, probably due to the saturation of cells grown on the culture dish. However, on day 5, cells grown on 100-nm nanodot arrays began to show a significant reduction in size.

The formation of focal adhesions reflected by the attachment of filopodia andlamellipodiato the substratum indicates healthy growth of cultured cells [34]. SEM images showed that the lamellar body of the migrating cells seeded on 50-nm nanodot arrays exhibited wide and thick features (Fig. 2). Cells seeded on flat surfaces and 10-nm nanodot arrays showed comparable lamellipodia. However, the cells seeded on 100-nm and 200-nm nanodos arrays are mounted with smaller size and narrow lamellipodia.

In summary, cells seeded on 50-nm nanodots showed the most extended morphology, including the largest surface area, most extended lamellipodia, and fastest growth rate. Cells grown on flat surfaces remained stable in the culture dish, while apoptosis-like growth and a significant reduction in the surface area were observed in cells cultured on the 100- and 200-nm nanodot arrays.

### 3.3. Cell adhesion and cytoskeletal organisation of cardiomyoblasts

Topography and surface chemistry may share a common pathway to direct cell behaviour. Cell adhesion is mediated through focal adhesions involving receptor-ligand binding [35]. To evaluate the role of adhesion molecules in nanotopography-induced apoptosis-like events, we immunostained cells grown on nanodot arrays for vinculin and actin filaments (Fig. 4). Vinculin is a membrane-bound cytoskeletal protein located in focal adhesion plaques that is involved in linkingintegrin adhesion molecules to the actin cytoskeleton. Vinculin staining indicated the formation of focal adhesions. Vinculin staining was widely distributed within cells grown on flat surfaces, 10-nm nanodot arrays, and, most prominently, 50-nm nanodot arrays. The amount of vinculin staining decreased or nearly vanished in cells grown on 100- or 200-nm nanodot arrays, respectively. Well-organised actin filaments were visible in cells grown on flat, 10-, and 50-nm nanodot arrays. This tight cytoskeletal arrangement was gradually lost and entirely disappeared for cells grown on 100- and 200-nm nanodot arrays, respectively.

Immunostaining indicated that nanodots smaller than 50-nm in diameter promoted protein expression related to cell adhesion and cytoskeletal organisation in cardiomyoblasts. Optimal adhesion occurred at 50-nm. Nanodots 100- and 200-nm in diameter reduced the formation of focal adhesions and inhibited the organisation of the cytoskeleton.

### 3.4. Expression of genes associated with cardiovascular function in cardiomyoblasts grown on varied nanotopographies

Heat shock proteins (Hsp) are involved in the cell response of heart disease. Hsp90 has been identified as a signalling molecule involved in the activation of all isoforms of nitric oxide synthase (iNOS). The present study showed that Hsp90, induced by mild heat shock treatment, can activate nitric oxide synthase enzymes (NOS) in cardiac H9c2 cells and result in production of nitric oxide (NO), a regulator of cell respiration [36]. The regulation of cellular respiration is directly related to many cardiovascular diseases. Periannan Kuppusamy's group has shown that the induction of Hsp90 during heat shock can activate NOS and increase NO production, thereby inhibiting respiration in cardiac H9c2 cells [37]. Quantitative PCR was performed to determine the levels of Hsp expression corresponding to various nanotopographies. As shown in Fig. 5a, mRNA levels of Hsp90 were significantly upregulated in cells cultured on 100-nm nanodot arrays. Expression

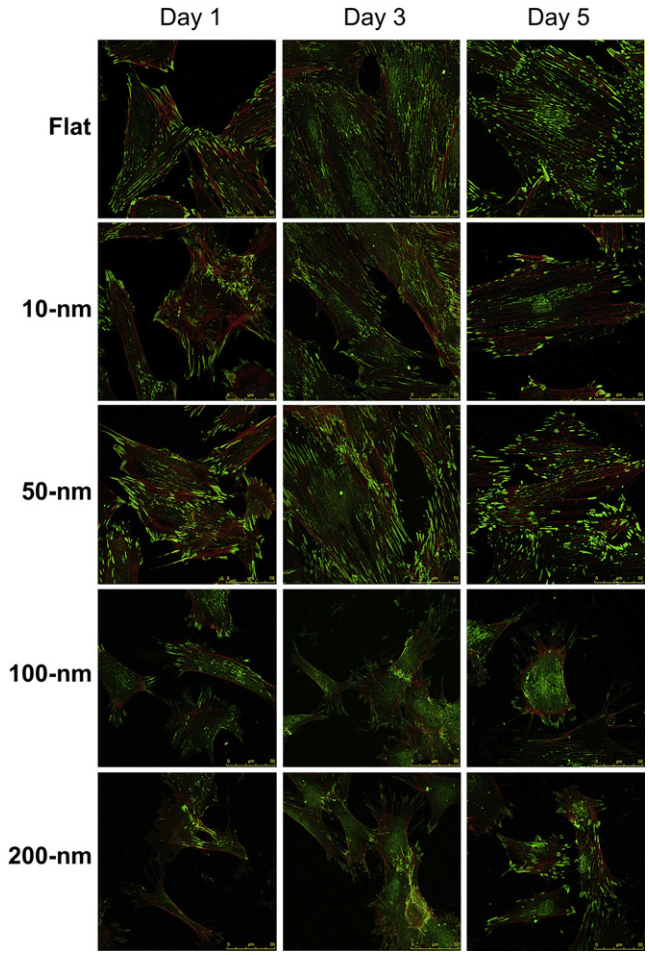


**Fig. 4.** Immunofluorescent staining shows distribution of vinculin (green) and actin filament (red) in H9c2 cells cultured on nanodot arrays. H9c2 cells were seeded on flat, 10-, 50-, 100-, and 200-nm nanodot arrays for 1, 3, or 5 days. Scale bar = 50 μm. (For interpretation of the references to colour in this figure legend, the reader is referred to the web version of this article.)

levels of Hsp70, Hsp60, and Hsp27 remained unchanged. Collectively, these data indicate that a stress response was induced in cells cultured on the 100-nm nanodot arrays.

Receptor activity-modifying proteins 2 and 3 (RAMP-2 and -3) are associated with increased vascular smooth muscle cell migration [38]. The expression of RAMP-2 or RAMP-3 mediates the inhibitory effect of adrenomedullin on cell migration. The high-affinity adrenomedullin receptor involved in the pathogenesis of cardiovascular diseases is composed of RAMP-2 and RAMP-3 [31]. Thus, RAMPs are key determinants of adrenomedullin-mediated effects on cell migration and are essential for angiogenesis and vascular integrity [39]. The mRNA levels of RAMP-2 and -3 increased for cardiomyoblasts seeded on 50- or 100-nm nanodot arrays (Fig. 5b). Nanotopography appeared to upregulate expression of RAMPs and control cell migration and the angiogenesis-like phenomenon.

Genes associated with apoptosis were also examined. The pro-apoptotic protein Bax plays an important role in cardiomyocyte cell death [40]. Overexpression of the anti-apoptotic Bcl-2 gene has been found in cardiac fibroblasts, which are well known to resist most situations that compromise cell survival [41]. Significant induction of Bcl-2 expression limits uncontrolled cell death [42]. The two genes, Bax and Bcl-2, play key roles in mitochondrial permeability and, thus, apoptosis [43]. The mRNA expression

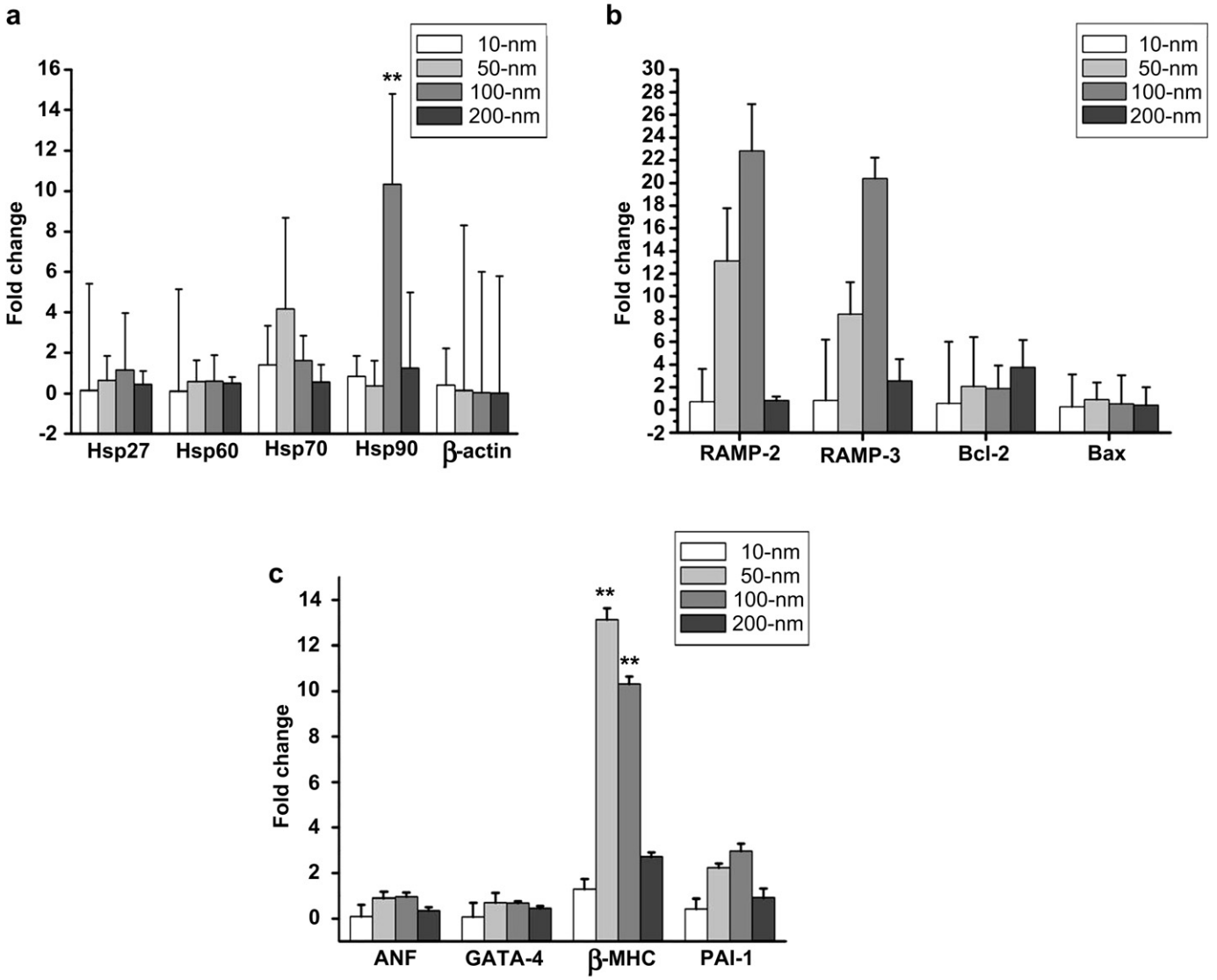


**Fig. 5.** qPCR of genes associated with heat shock, apoptosis, hypertrophy, and fibrosis in H9c2 cardiomyoblasts. H9c2 cells were cultured on flat, 10-, 50-, 100-, and 200-nm nanodot arrays for 3 days before qPCR was performed. (a) Hsp90, Hsp70, Hsp60, Hsp27 and β-actin expression. (b) RAMP-2, RAMP-3, Bcl-2, and Bax expression. (c) ANF, GATA-4, β-MHC, and PAI-1 expression. The mean ± SD from at least 3 experiments is shown. $^{*}p < 0.05$ and $^{**}p < 0.01$ when compared with flat control surfaces.

profile of Bcl-2 and Bax observed in H9c2 cardiomyoblasts cultured on different nanotopographies were determined using qPCR (Fig. 5b). The lack of an apparent difference in Bcl-2 and Bax expression indicated that these two genes were less correlated to the topography-induced apoptotic pathways.

The characteristic features of cardiac hypertrophy include increased cell area, enhanced cytoskeletal organisation, elevated cardiac gene expression, and upregulated atrial natriuretic factor (ANF) and beta myosin heavy chain (β-MHC) [44]. PAI-1 inhibits extracellular matrix-degrading metalloproteinases and promotes fibrosis in neonatal rat cardiomyoblasts and H9c2 rat cardiomyoblasts [45]. The transcription factor GATA-4, a master regulator of cardiac genes, has been implicated in both the transcriptional activation of genes encoding ANF and contractile proteins and the sarcomeric reorganisation response to hypertrophic stimulation [46].

We measured the expression of hypertrophy-associated genes, including PAI-1, β-MHC, GATA-4, and ANF, in cardiomyoblasts cultured on various nanotopographies. As shown in Fig. 5c, the mRNA levels of PAI-1 and β-MHC were significantly enhanced in cells cultured on 50- and 100-nm nanodot arrays. The expression levels of GATA-4 and ANF remained unchanged.

The mRNA expression levels of PAI-1 and β-MHC increased in cardiomyoblasts that were seeded on 50- and 100-nm nanodot arrays. Arrays of 50 and 100 nm-diameter nanodots may promote hypertrophic and fibrotic processes in cultured cardiomyoblasts.

### *3.5. Western blotting and confirmation of the topological control of PAI-1 and vinculin expression*

Nanotopography controls the cell adhesion and cellular function of cardiomyoblasts. Western blots were performed to validate the expression of vinculin and PAI-1 proteins (Fig. 6a). Cell spreading and migration occur though the binding of cell surface integrin receptors to extracellular matrixadhesion molecules. Vinculin is associated with focal adhesions and adherens junctions, both of which connect actin filaments and crosslinkers between the

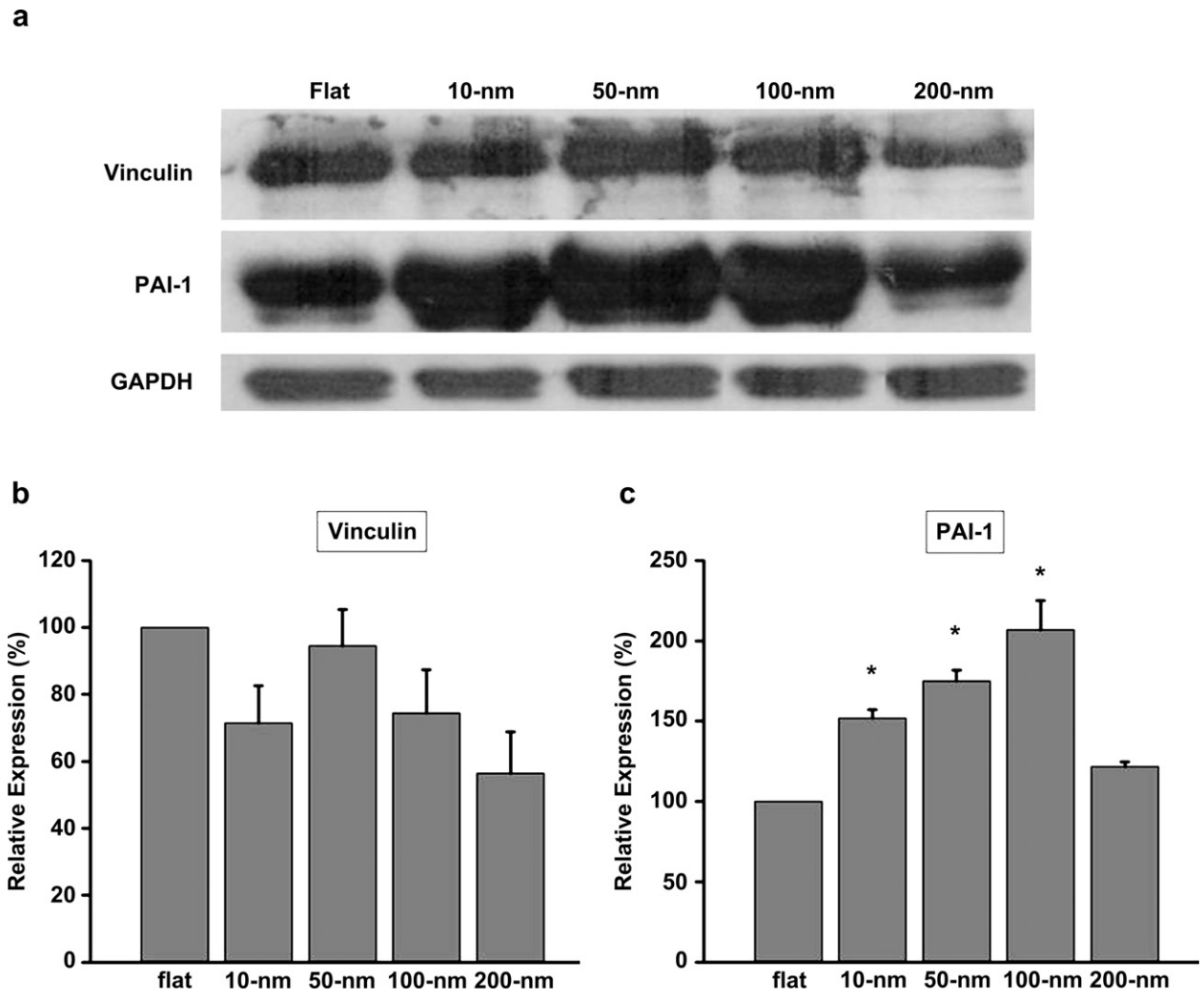


**Fig. 6.** Protein expression of H9c2 on nanodot arrays (a) Western blots analysis of vinculin and PAI-1 for H9c2 cells cultured on nanodot arrays. Cardiomyoblasts were collected after 3 days culture. (b) Relative density of vinculin expression versus nanodot size. (c) Relative density of PAI-1 expression versus nanodot size. The densitometric analysis of each band was performed and relative density calculated using expression of GAPDH as a control. The mean ± SD from at least 3 experiments is shown. $^{*}p < 0.05$ when compared with flat control surfaces.

external medium, plasma membrane, and actin cytoskeleton [47]. In the immunofluorescence experiments, vinculin staining reached maximum for cells cultured on 50-nm nanodot arrays. Based on western blot results, the highest level of expression occurred in cells cultured on 50-nm nanodot arrays (Fig. 6b). The levels of PAI-1 were enhanced significantly in cardiomyoblasts seeded on 50-nm nanodot arrays (Fig. 6c). Although the 50-nm nanodot array surface enhanced cell growth and adhesion, it also promoted the risk of hypertrophic stimulation and fibrosis in cardiomyoblasts.

## 4. Conclusion

In this study, we showed that nanotopography can control the growth and function of cardiomyoblasts. Differential growth of cardiomyoblasts on nanodot arrays was demonstrated. The optimal growth, most extended morphology, largest surface area, and greatest proliferation occurred in cells cultured on 50 nm nanodot arrays. Implants fabricated using similar surfaces are anticipated to have better biocompatibility and be more suited to long-term function in the human body. The nanotopography of the 100- and 200-nm nanodot arractivity–modifying proteinsays reduced cell growth and attachment, thus inducing apoptosis in cells. qPCR showed that 50- and 100-nm nanodot arrays can induce fibrosis for H9c2 cardiomyoblasts. Nanodots of 100- and 200-nm in diameter could be incorporated into the surface of implants to purposely inhibit cell growth.

## Acknowledgements

This paper (work) was supported by "Aim for the Top University Plan" of the National Chiao Tung University and Ministry of Education, Taiwan, R.O.C.

## References

[1] Choudhary S, Haberstroh KM, Webster TJ. Enhanced functions of vascular cells on nanostructured Ti for improved stent applications. Tissue Eng 2007;13:1421–30.
[2] Robertson SW, Imbeni V, Wenk HR, Ritchie RO. Crystallographic texture for tube and plate of the superelastic/shape-memory alloy Nitinol used for endovascular stents. J Biomed Mater Res A 2005;72:190–9.
[3] Verheye S, Markou CP, Salame MY, Wan B, King 3rd SB, Robinson KA, et al. Reduced thrombus formation by hyaluronic acid coating of endovascular devices. Arterioscler Thromb Vasc Biol 2000;20:1168–72.
[4] Chen JY, Leng YX, Tian XB, Wang LP, Huang N, Chu PK, et al. Antithrombogenic investigation of surface energy and optical bandgap and hemocompatibility mechanism of Ti(Ta(+5))O2 thin films. Biomaterials 2002;23:2545–52.

[5] Dolmatch B, Dong YH, Heeter Z. Evaluation of three polytetrafluoroethylene stent-grafts in a model of neointimal hyperplasia. J Vasc Interv Radiol 2007; 18:527–34.
[6] Schuler P, Assefa D, Ylanne J, Basler N, Olschewski M, Ahrens I, et al. Adhesion of monocytes to medical steel as used for vascular stents is mediated by the integrin receptor Mac-1 (CD11b/CD18; alphaM beta2) and can be inhibited by semiconductor coating. Cell Commun Adhes 2003;10:17–26.
[7] Achneck HE, Jamiolkowski RM, Jantzen AE, Haseltine JM, Lane WO, Huang JK, et al. The biocompatibility of titanium cardiovascular devices seeded with autologous blood-derived endothelial progenitor cells: EPC-seeded antithrombotic Ti implants. Biomaterials 2011;32:10–8.
[8] Stevens MM, George JH. Exploring and engineering the cell surface interface. Science 2005;310:1135–8.
[9] Miller DC, Haberstroh KM, Webster TJ. Mechanism (s) of increased vascular cell adhesion on nanostructured poly (lactic co glycolic acid) films. J Biomed Mater Res A 2005;73:476–84.
[10] Miller DC, Thapa A, Haberstroh KM, Webster TJ. Endothelial and vascular smooth muscle cell function on poly (lactic-co-glycolic acid) with nano-structured surface features. Biomaterials 2004;25:53–61.
[11] Berry C, McCloy D, Affrossman S. Endothelial cell response to narrow diameter nylon tubes exhibiting internal nanotopography. Curr Nanoscience 2008;4: 219–23.
[12] Biggs MJP, Richards RG, Dalby MJ. Nanotopographical modification: a regulator of cellular function through focal adhesions. Nanomedicine 2010;6:619–33.
[13] Lee J, Chu BH, Chen KH, Ren F, Lele TP. Randomly oriented, upright SiO2 coated nanorods for reduced adhesion of mammalian cells. Biomaterials 2009;30:4488–93.
[14] Tooley WW, Feghhi S, Han SJ, Wang J, Sniadecki NJ. Thermal fracture of oxidized polydimethylsiloxane during soft lithography of nanopost arrays. J Micromech Microeng 2011;21:054013.
[15] Dalby MJ, Giannaras D, Riehle MO, Gadegaard N, Affrossman S, Curtis AS. Rapid fibroblast adhesion to 27nm high polymer demixed nano-topography. Biomaterials 2004;25:77–83.
[16] Dalby MJ, Riehle MO, Sutherland DS, Agheli H, Curtis AS. Fibroblast response to a controlled nanoenvironment produced by colloidal lithography. J Biomed Mater Res A 2004;69:314–22.
[17] Lee J, Kang BS, Hicks B, Chancellor TF, Chu BH, Wang HT, et al. The control of cell adhesion and viability by zinc oxide nanorods. Biomaterials 2008;29: 3743–9.
[18] Choi CH, Hagvall SH, Wu BM, Dunn JCY, Beygui RE, "Cj" Kim CJ. Cell interaction with three-dimensional sharp-tip nanotopography. Biomaterials 2007;28:1672–9.
[19] Ahmed I, Ponery AS, Nur EKA, Kamal J, Meshel AS, Sheetz MP, et al. Morphology, cytoskeletal organization, and myosin dynamics of mouse embryonic fibroblasts cultured on nanofibrillar surfaces. Mol Cell Biochem 2007;301:241–9.
[20] Hehrlein C, Zimmermann M, Metz J, Ensinger W, Kubler W. Influence of surface texture and charge on the biocompatibility of endovascular stents. Coron Artery Dis 1995;6:581–6.
[21] Cremonesi A, Benit E, Carlier M, Colombo A, Piva R, Probst P, et al. Multicenter registry to evaluate the efficacy of the NIROYAL stent in de novo or restenotic coronary stenosis. J Invasive Cardiol 2000;12:225–32.
[22] Hoffmann R, Mintz GS, Haager PK, Bozoglu T, Grube E, Gross M, et al. Relation of stent design and stent surface material to subsequent in-stent intimal hyperplasia in coronary arteries determined by intravascular ultrasound. Am J Cardiol 2002;89:1360–4.
[23] Aspenberg P, Anttila A, Konttinen YT, Lappalainen R, Goodman SB, Nordsletten L, et al. Benign response to particles of diamond and SiC: bone chamber studies of new joint replacement coating materials in rabbits. Biomaterials 1996;17:807–12.
[24] Heublein B, Ozbek C, Pethig K. Silicon carbide-coated stents: clinical experience in coronary lesions with increased thrombotic risk. J Endovasc Surg 1998;5:32–6.
[25] Babapulle MN, Eisenberg MJ. Coated stents for the prevention of restenosis: part II. Circulation 2002;106:2859–66.
[26] Caves JM, Chaikof EL. The evolving impact of microfabrication and nanotechnology on stent design. J Vasc Surg 2006;44:1363–8.
[27] Doyle B, Rihal CS, O'Sullivan CJ, Lennon RJ, Wiste HJ, Bell M, et al. Outcomes of stent thrombosis and restenosis during extended follow-up of patients treated with bare-metal coronary stents. Circulation 2007;116:2391–8.
[28] Hung YC, Pan HA, Tai SM, Huang GS. A nanodevice for rapid modulation of proliferation, apoptosis, invasive ability, and cytoskeletal reorganization in cultured cells. Lab Chip 2010;10:1189–98.
[29] Pan HA, Hung YC, Su CW, Tai SM, Chen CH, Ko FH, et al. A nanodot array modulates cell adhesion and induces an apoptosis-like abnormality in NIH-3T3 cells. Nanoscale Res Lett 2009;4:903–12.
[30] Cetrullo S, Facchini A, Stanic I, Tantini B, Pignatti C, Caldarera CM, et al. Difluoromethylornithine inhibits hypertrophic, pro-fibrotic and pro-apoptotic actions of aldosterone in cardiac cells. Amino Acids 2010;38:525–31.
[31] Sueur S, Pesant M, Rochette L, Connat JL. Antiapoptotic effect of calcitonin gene-related peptide on oxidative stress-induced injury in H9c2 cardiomyocytes via the RAMP1/CRLR complex. J Mol Cell Cardiol 2005;39: 955–63.
[32] Wang H, Lin G, Zhang Z. ATF5 promotes cell survival through transcriptional activation of Hsp27 in H9c2 cells. Cell Biol Int 2007;31:1309–15.
[33] Wu CT, Ko FH, Hwang HY. Self-aligned tantalum oxide nanodot arrays through anodic alumina template. Microelectronic Eng 2006;83:1567–70.
[34] Partridge MA, Marcantonio EE. Initiation of attachment and generation of mature focal adhesions by integrin-containing filopodia in cell spreading. Mol Biol Cell 2006;17:4237–48.
[35] Andersson AS, Backhed F, von Euler A, Richter-Dahlfors A, Sutherland D, Kasemo B. Nanoscale features influence epithelial cell morphology and cytokine production. Biomaterials 2003;24:3427–36.
[36] Harris MB, Ju H, Venema VJ, Blackstone M, Venema RC. Role of heat shock protein 90 in bradykinin-stimulated endothelial nitric oxide release. Gen Pharmacol 2000;35:165–70.
[37] Ilangovan G, Osinbowale S, Bratasz A, Bonar M, Cardounel AJ, Zweier JL, et al. Heat shock regulates the respiration of cardiac H9c2 cells through upregulation of nitric oxide synthase. Am J Physiol Cell Physiol 2004;287:C1472–81.
[38] Fukai N, Shichiri M, Ozawa N, Matsushita M, Hirata Y. Coexpression of calcitonin receptor-like receptor and receptor activity-modifying protein 2 or 3 mediates the antimigratory effect of adrenomedullin. Endocrinology 2003; 144:447–53.
[39] Ichikawa-Shindo Y, Sakurai T, Kamiyoshi A, Kawate H, Iinuma N, Yoshizawa T, et al. The GPCR modulator protein RAMP2 is essential for angiogenesis and vascular integrity. J Clin Invest 2008;118:29–39.
[40] Hou Q, Hsu YT. Bax translocates from cytosol to mitochondria in cardiac cells during apoptosis: development of a GFP-Bax-stable H9c2 cell line for apoptosis analysis. Am J Physiol Heart Circ Physiol 2005;289:H477–87.
[41] Mayorga M, Bahi N, Ballester M, Comella JX, Sanchis D. Bcl-2 is a key factor for cardiac fibroblast resistance to programmed cell death. J Biol Chem 2004;279: 34882–9.
[42] Kutschka I, Kofidis T, Chen IY, von Degenfeld G, Zwierzchoniewska M, Hoyt G, et al. Adenoviral human BCL-2 transgene expression attenuates early donor cell death after cardiomyoblast transplantation into ischemic rat hearts. Circulation 2006;114:I-174–80.
[43] Sharpe JC, Arnoult D, Youle RJ. Control of mitochondrial permeability by Bcl-2 family members. Biochim Biophys Acta 2004;1644:107–13.
[44] Watkins SJ, Borthwick GM, Arthur HM. The H9C2 cell line and primary neonatal cardiomyocyte cells show similar hypertrophic responses in vitro. In Vitro Cell Dev Biol Anim 2010;47:125–31.
[45] Tanaka K, Ashizawa N, Kawano H, Sato O, Seto S, Nishihara E, et al. Aldosterone induces circadian gene expression of clock genes in H9c2 cardiomyoblasts. Heart Vessels 2007;22:254–60.
[46] Laverriere AC, MacNeill C, Mueller C, Poelmann RE, Burch JB, Evans T. GATA-4/5/6, a subfamily of three transcription factors transcribed in developing heart and gut. J Biol Chem 1994;269:23177–84.
[47] Xu W, Baribault H, Adamson ED. Vinculin knockout results in heart and brain defects during embryonic development. Development 1998;125:327–37.